JOURNAL OF PROPULSION AND POWER
Vol. 26, No. 5, September–October 2010

Large-Eddy Simulation of Flame–Turbulence Interactions in a Shear Coaxial Injector

Matthieu Masquelet* and Suresh Menon†
Georgia Institute of Technology, Atlanta, Georgia 30332-0150

DOI: 10.2514/1.48023

The turbulent combustion inside the main chamber of a liquid rocket engine is difficult to numerically model because of the wide range of scales involved, the complex thermodynamics at elevated pressure, and the influence of heat transfer. Here, a single-element gaseous-hydrogen–gaseous-oxygen shear-coaxial injector is studied. This case involves complex physical processes that are simulated using a large-eddy simulation approach. In particular, modeling of the nonpremixed turbulent combustion and its impact on the wall heat flux is addressed. This large-eddy simulation of the compressible multispecies Navier–Stokes equations is solved using a hybrid central-upwind scheme with a thermally perfect formulation. To keep the computational cost reasonable, priority was given to the near-field resolution over the near-wall resolution. The modeled flame anchoring and dynamics provide a satisfactory estimate of the wall heat flux. The unsteady and three-dimensional features of the flow are discussed in length, and the implications of the unique features of this shear-coaxial GH_2-GO_2 injector for turbulent combustion modeling are analyzed.

Nomenclature

C_ϵ, C_ν	=	model coefficients for the subgrid closure
$\mathcal{D}$	=	mass diffusivity, $m^2 \cdot s^{-1}$
e_T	=	total energy (internal + kinetic) per unit mass, $J \cdot kg^{-1}$
H^{sgs}	=	subgrid enthalpy flux, $J \cdot m^{-2}$
h_k	=	partial massic enthalpy of species k, $J \cdot kg^{-1}$
J_k	=	mass diffusion flux, $kg \cdot m^{-2}$
k^{sgs}	=	turbulent kinetic energy, $m^2 \cdot s^{-2}$
N_S	=	number of species considered
P^{sgs}	=	production of turbulent kinetic energy, $kg \cdot m^{-1} \cdot s^{-3}$
p	=	pressure, pa
Q_{IK}	=	heat flux in the Irving–Kirkwood form, $J \cdot m^{-2}$
Q_k^{sgs}	=	subgrid enthalpy flux due to diffusion of species k, $J \cdot m^{-2}$
R	=	gas constant, $J \cdot kg^{-1} \cdot K^{-1}$
T	=	temperature, k
t	=	time, s
u	=	velocity, $m \cdot s^{-1}$
$\mathcal{V}_k$	=	diffusion velocity of species k, $m \cdot s^{-1}$
x_i	=	Cartesian coordinate, m
Y_k	=	mass fraction of species k
Δ	=	grid filter size, m
ϵ^{sgs}	=	subgrid dissipation of turbulent kinetic energy, $kg \cdot m^{-1} \cdot s^{-3}$
θ_k^{sgs}	=	subgrid species diffusive flux, $kg \cdot m^{-2}$
λ	=	thermal conductivity, $W \cdot m^{-1} \cdot K^{-1}$
μ	=	dynamic viscosity, $Pa \cdot s$
ρ	=	density, $kg \cdot m^{-3}$
σ^{sgs}	=	subgrid heat flux, $J \cdot m^{-2}$
τ_{ij}	=	stress tensor

Subscripts

i, j	=	Cartesian direction
k	=	species k property
m	=	mixture property

Superscripts

$\bar{x}$	=	spatially filtered quantity
$\tilde{x}$	=	Favre-filtered quantity
x^{sgs}	=	subgrid quantity

I. Introduction

WITH the retirement of the space shuttle planned for 2010 and a renewed worldwide interest in space exploration, there is a need to leverage past experience and increasingly affordable computational power to help design the next generation of rocket engines. Past designs were developed with very expensive experimental test campaigns, amid a lot of trial and error. For the future, it is desirable to use the predictive and analytical capabilities of computational fluid dynamics (CFD) to limit the amount of experiments needed during the development phase of a new engine. One of the first attempts to formalize this new approach can be credited to Tucker et al. [1]. Their configuration of choice for a joint numerical and experimental effort of rocket engine modeling validation was a single-element gas–gas shear-coaxial injector. The flow produced by this geometry is one of the simplest ones for rocket injection. It is yet very relevant for the U.S. space program, given the staged combustion cycle of the space shuttle main engine.

Liquid-gas injectors are more frequently found in space vehicles; thus, a significant amount of the recent literature has been focusing on these configurations. For example, there has been a large effort focusing on single-element injectors such as the Mascotte test bench [2,3] or the experiments at DLR, German Aerospace Research Center in Germany [4–6]. Multielement configurations such as the Astrium test case [7] have also started to be investigated using unsteady simulations [8] even though their inherent computational cost limits the complexity of the modeling efforts. These injectors produce even more complex physics than the simple gas–gas shear-coaxial injector through their multiphase nature or the importance of the real gas effects for subcritical or supercritical injection. But CFD solvers have not yet been able to satisfy requirements of robustness, fidelity and accuracy on simpler gas–gas shear-coaxial injectors [9]

Presented as Paper 2008-5030 at the 44th AIAA/ASME/SAE/ASEE Joint Propulsion Conference and Exhibit, Hartford, CT, 21–23 July 2008; received 6 November 2009; revision received 15 March 2010; accepted for publication 15 March 2010.

*Graduate Research Assistant, Computational Combustion Laboratory, School of Aerospace Engineering; gtg540e@mail.gatech.edu. Student Member AIAA.

†Professor, Director of Computational Combustion Laboratory, School of Aerospace Engineering; suresh.menon@ae.gatech.edu. Associate Fellow AIAA.

in order to be fully validated as useful design help in a production environment.

It is important to stress the differences between these gas–gas shear-coaxial rocket injectors and more common turbulent nonpremixed jet flames extensively studied in laboratories. The large inlet velocities of the rocket injectors not only produce high levels of turbulence, they also make the flow quite compressible, as opposed to the nearly incompressible jet flames usually studied. Also, despite the high strain rates, the low levels of dilution as well as the elevated pressure mean the flame is not lifted as in some similar hydrogen experimental flames [10]. Finally, if hydrogen–oxygen injectors are considered, the available experimental data is very limited under realistic rocket conditions because of the environment inside the chamber. The two most recent works by Marshall et al. [11] and Conley et al. [12] only provide quantitative data for the heat flux along the outer wall of the chamber. Conley et al. also obtained some limited flame visualization, and their configuration will need to be investigated in the future, even though the smaller physical dimensions of the injector increase the range of scales to be considered and, thus, the computational cost.

As part of a NASA evaluation of various state-of-the-art solvers [13], the Pennsylvania State University (PSU)-RCM1 rig studied by Marshall et al. [11] was chosen for validation purposes. This paper highlights the results obtained with a large-eddy simulation (LES) approach and focuses on the physics of the nonpremixed turbulent flame occurring under realistic rocket engine operating conditions. It is organized as follows: the next section presents the numerical model and the various closure approximations employed, then the configuration of interest is introduced along with the computational grid and boundary conditions, and, finally, results are presented in which unsteady and three-dimensional (3-D) features are highlighted.

II. Formulation

The current simulation solves the Favre-filtered compressible multispecies and unsteady Navier–Stokes equations in conservative form. Following Erlebacher et al. [14], the flow variables are decomposed by a spatial filtering operation (denoted by $\bar{f}$) and two separate fields are obtained: the unresolved (or subgrid) scale and the resolved (or supergrid) scale, represented by a tilde ($\tilde{f} = \overline{\rho f}/\bar{\rho}$). The filtered equations, respectively, for mass conservation [Eq. (1)], momentum conservation [Eq. (2)], energy conservation [Eq. (3)], and species conservation [Eq. (4)] are solved simultaneously to obtain the conservative filtered variables:

$$\frac{\partial \bar{\rho}}{\partial t} + \frac{\partial \bar{\rho}\tilde{u}_i}{\partial x_i} = 0 \tag{1}$$

$$\frac{\partial \bar{\rho}\tilde{u}_i}{\partial t} + \frac{\partial}{\partial x_j}(\bar{\rho}\tilde{u}_i\tilde{u}_j + \bar{p}\delta_{ij} - \bar{\tau}_{ij} + \tau_{ij}^{\text{sgs}}) = 0 \tag{2}$$

$$\frac{\partial \bar{\rho}\tilde{e}^T}{\partial t} + \frac{\partial}{\partial x_i}(\bar{\rho}\tilde{e}_T\tilde{u}_i + \bar{p}\tilde{u}_i + \bar{Q}_{i,\text{IK}} - \tilde{u}_j\bar{\tau}_{ji} + H_i^{\text{sgs}} + \sigma_i^{\text{sgs}}) = 0 \tag{3}$$

$$\frac{\partial \bar{\rho}\tilde{Y}_k}{\partial t} + \frac{\partial}{\partial x_i}(\bar{\rho}\tilde{Y}_k\tilde{u}_i + \bar{J}_{i,k} + Y_{i,k}^{\text{sgs}} + \theta_{i,k}^{\text{sgs}}) = \bar{\dot{\omega}}_k \quad \text{for } k = 1, \ldots, N_S \tag{4}$$

However, several quantities other than the primitive and conservative variables have been introduced in the above equations and require closure. The heat diffusion flux (shown in Eqs. (3) and (5) in its Irving–Kirkwood form, including the enthalpy flux by mass diffusion) and the mass diffusion flux [Eq. (6)] are solely based on Fick's and Fourier's types of diffusion:

$$\bar{Q}_{i,\text{IK}} = -\bar{\lambda}\frac{\partial \tilde{T}}{\partial x_i} + \bar{\rho}\sum_{k=1}^{N_S}\tilde{h}_k\tilde{Y}_k\tilde{\mathcal{V}}_{i,k} + \sum_{k=1}^{N_S}Q_{i,k}^{\text{sgs}} \tag{5}$$

$$\bar{J}_{i,k} = \bar{\rho}\tilde{Y}_k\tilde{\mathcal{V}}_{i,k} = -\bar{\rho}\bar{\mathcal{D}}_{k,m}\frac{\partial \tilde{Y}_k}{\partial x_i} \tag{6}$$

with the approximation of evaluating the diffusion coefficient $\mathcal{D}_{k,m}$ of each species into the mixture instead of considering each individual binary diffusion. Thus, the cross-diffusion Dufour and Soret terms are neglected in this study. Despite the elevated pressure inside the PSU rig, the conditions are far from being supercritical and these cross-diffusion terms are inherently small (less than 10% of the heat/mass fluxes). While they could promote intermittency and flame extinction, resulting in a slight decrease of the flame temperature, even detailed direct numerical simulation studies of mixing layers have not reached a definitive conclusion on their importance [15,16].

The subgrid species diffusive flux $\theta_{i,k}^{\text{sgs}} = \bar{\rho}(\widetilde{\mathcal{V}_{i,k}Y_k} - \tilde{\mathcal{V}}_{i,k}\tilde{Y}_k)$ is usually neglected because it has been shown to have a small magnitude at high Reynolds numbers [17,18], such as the ones found in the main shear layers of the current injector flow. The subgrid enthalpy flux H_i^{sgs} and the subgrid heat flux $\sigma_i^{\text{sgs}} = -(\overline{u_j\tau_{ji}} - \tilde{u}_j\bar{\tau}_{ji})$ are modeled together:

$$H_i^{\text{sgs}} + \sigma_i^{\text{sgs}} = -(\bar{\rho}\bar{\nu}_t + \bar{\mu})\frac{\partial k^{\text{sgs}}}{\partial x_i} - \frac{\bar{\rho}\bar{\nu}_t c_p}{Pr_t}\frac{\partial \tilde{T}}{\partial x_i} + \tilde{u}_j\tau_{ij}^{\text{sgs}} \tag{7}$$

The subgrid stress tensor $\tau_{ij}^{\text{sgs}} = \bar{\rho}(\widetilde{u_iu_j} - \tilde{u}_i\tilde{u}_j)$, the subgrid enthalpy flux due to mass diffusion $Q_{i,k}^{\text{sgs}} = \bar{\rho}(h_k\widetilde{\mathcal{V}_{i,k}Y_k} - \tilde{h}_k\tilde{\mathcal{V}}_{i,k}\tilde{Y}_k)$ and the subgrid species flux $Y_{i,k}^{\text{sgs}} = \bar{\rho}(\widetilde{u_iY_k} - \tilde{u}_i\tilde{Y}_k)$, are closed using a gradient diffusion approach and a subgrid eddy viscosity that uses the turbulent kinetic energy [19].

The momentum closure employs an eddy viscosity closure and an additional transport equation is needed for the turbulent kinetic energy $k^{\text{sgs}} = \frac{1}{2}(\widetilde{u_iu_i} - \tilde{u}_i\tilde{u}_i)$. Assuming a simple gradient diffusion model for the subgrid transport, this equation reads:

$$\frac{\partial \bar{\rho}k^{\text{sgs}}}{\partial t} + \frac{\partial}{\partial x_i}(\bar{\rho}k^{\text{sgs}}\tilde{u}_i) = P^{\text{sgs}} - \epsilon^{\text{sgs}} - \frac{\partial}{\partial x_i}\left(\bar{\rho}\frac{(\bar{\nu} + \bar{\nu}_t)}{Pr_t}\frac{\partial k^{\text{sgs}}}{\partial x_i}\right) \tag{8}$$

The expressions for the production $P^{\text{sgs}} = -\tau_{ij}^{\text{sgs}}(\partial\bar{u}_i/\partial x_j)$ and dissipation $\epsilon^{\text{sgs}} = C_\epsilon\bar{\rho}(\sqrt{(k^{\text{sgs}})^3}/\Delta)$ terms leave only two model coefficients, C_ν and C_ϵ, to complete the subgrid closure. A localized dynamic procedure [20,21] is available in the current flow solver to compute these coefficients, as well as the turbulent Prandtl and Schmidt numbers. As a first approximation, constant classical values of 0.067 and 0.916 for C_ν and C_ϵ will be used in the current study unless mention of the dynamic procedure is explicitly made. These values were evaluated in earlier studies [22] without any a priori assumptions of ideal gas behavior but assuming incompressible flows. The turbulent Prandtl and Schmidt numbers are assumed constant in the current study as, respectively, 0.9 and 0.7. This follows generally accepted values in the literature although these numbers can display relatively large fluctuations [23,24].

All the subgrid terms have now been closed and the filtered pressure is computed through the filtered ideal gas equation of state, $\bar{p} = \bar{\rho}\tilde{R}_m\tilde{T}$, assuming the subgrid temperature–species correlation,

$$\sum_{k=1}^{N_S}\tilde{R}_k(\widetilde{Y_kT} - \tilde{Y}_k\tilde{T})$$

can be neglected [18]. Thermodynamic quantities such as specific heats, enthalpy or internal energy are computed using classical temperature curve fits [25]. Transport properties such as the viscosity μ and thermal conductivity λ are also computed using species-specific temperature curve fits, as well as Wilke's law [26], to compute the mixture average. The mixture averaged diffusion coefficient for each species is approximated as $\mathcal{D}_{k,m} = \lambda_m/c_{p,m}/Le_k$, with a different Lewis number Le for each species. This completes the multispecies, thermally perfect formulation. Finite-rate chemistry is modeled using a high-pressure hydrogen–oxygen mechanism consisting of 21 elementary steps among eight species [27]: O_2, H_2, OH, O, H, H_2O_2, H_2O, HO_2. It is a significant improvement

compared with simpler mechanisms previously used in similar rocket engines configurations [28,29]. However, the stiffness of this mechanism makes it especially hard to integrate numerically. There is also the added complexity of the closure of the chemical source term in the species conservation equation. In the end, a laminar closure model is chosen, coupled with a subiteration scheme for time integration of the reaction rates. This choice is analyzed in the Results section.

III. GH_2-GO_2 Shear-Coaxial Injector

The single-element shear-coaxial injector investigated by the PSU in their cryogenic combustion laboratory is the focus of this study. This small-scale thrust chamber consists of oxidizer and fuel preburners providing the two streams of reactants for the coaxial injector and is part of the NASA's Marshall Center validation campaign and the Constellation Universities Institutes Project (CUIP) [30]. The combustor, referred to as PSU-RCM1, is composed of a cylindrical chamber instrumented for wall heat flux measurement and a convergent–divergent nozzle. A detailed description of the experimental setup is given in a previous paper [31], whereas additional details on the instrumentation and the measured data can be found elsewhere [11,32]. A schematic of the rig is shown in Fig. 1 alongside the wall temperatures used for the isothermal wall simulations.

Of note, while the target chamber pressure is high (5.5 MPa), the injection temperatures of the reactants (711 K for the oxidizer stream and 800 K for the fuel stream) prevent any significant real gas effects to occur and justify the use of the perfect gas equation of state in the simulations. Operating conditions and the geometry of the injector reflect those found in an actual staged combustion engine. For reference, the inlet Mach numbers are 0.29 and 0.51 for the oxidizer and fuel post exits, and the Reynolds numbers there are (respectively) 650,000 and 150,000.

Since direct measurements inside the chamber are very difficult under such conditions, the main validation data available is the wall heat flux along the cylindrical part of the combustion chamber. Also, while the volume of the chamber is small enough to require active cooling, the distance between the injector centerline and the chamber wall is about twice as large (19 mm) as in a real engine [33]. Thus, the flow confinement experienced in a multi-injector configuration is not correctly represented, with the flow conditions along the wall being significantly different. For example, the large recirculation in the corner of the chamber is unlikely to be present in an actual configuration.

Finally, while the wall heat flux is the only available experimental data, it will not be the primary focus of this study. Because of assumptions in the formulation and the grid resolution employed (detailed later), it is acknowledged that the prediction of this wall heat flux, although reasonable, could be improved. The main goal of this study is to demonstrate the ability of the unsteady, 3-D LES approach to capture the overall physics of a typical rocket injector flame.

IV. Numerical Setup

A. Implementation

The staged combustion nature of the PSU-RCM1 rig not only allows the use of the perfect gas equation of state as mentioned in the previous section, it also limits the density gradients between the streams of the reactants at the inflow. In previous works related to cryogenic injection of H_2 and O_2 [29], the limitations of a central scheme used by the flow solver were highlighted when dealing with such large density gradients. While the density ratio between the injected streams is only about 10 for the present case (compared with well over 100 for a cryogenic injection), preliminary testing has clearly shown the necessity of running a hybrid central-upwind scheme instead of a pure central scheme.

The current fully compressible flow solver uses a finite-volume scheme with a second-order time-accurate predictor–corrector integration and a second-order accurate hybrid solver for spatial integration. This finite-volume hybrid solver alternates between a second-order central scheme and a third-order accurate MUSCL, an upwind-biased scheme. A dynamic and local switch [34], based on pressure and density gradients, determines (at each time step and each computational face) which scheme to use. The MUSCL reconstruction technique is used alongside an approximate Riemann solver (specifically, Harten–Lax–van Leer (HLL) from Génin and Menon [35], with HLL contact/solver modifications by Toro et al. [36]), as well as the monotonized central limiter [37], to enforce the total variation diminishing condition. This hybrid scheme allows the capture of the large density gradients typically found near the

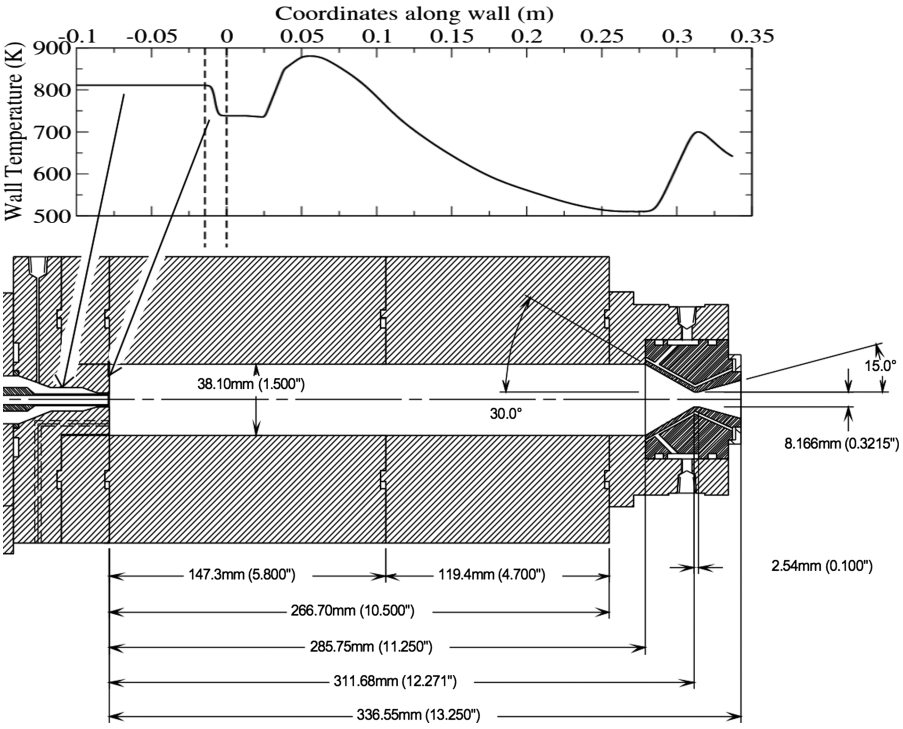

Fig. 1 Schematic of the RCM1 combustor [32], with a graph of the temperature alongside the outer wall of the rig. Coordinates along the wall correspond to the distance from the injection plane for the chamber wall. Arrows indicate which wall corresponds to which part of the profile.

injection plane while keeping the required grid resolution reasonable and keeping the less-dissipative central scheme in the far field in order to accurately model the turbulence.

Characteristic inflow with constant mass flux and supersonic outflow boundary conditions are employed, respectively, at both fuel and oxidizer inlets and for the choked nozzle. Isothermal conditions along the combustor wall use the experimental wall temperature profile and, for the injector walls (including the injector plate), a blended function is used to smoothly go from the injection temperature to the external wall temperature. With the flame expected to sit near the tip of the oxygen post, the wall temperature there is set at about the highest possible temperature sustainable for the wall material, that is 900 K. These boundary conditions are illustrated in Fig. 1. Assuming a near uniform grid normal to the wall, the temperature gradient at the wall can be computed as

$$\left(\frac{\partial T}{\partial y}\right)_{\text{wall}} = \frac{-9T_j + 8T_{\text{wall}} + T_{j-1}}{3\Delta y}$$

The heat flux is then obtained by multiplying this gradient by the sum of the molecular and turbulent thermal conductivities, as seen in Eqs. (5) and (7). Given the wall resolution of the current simulations, the turbulent contribution dominates along the outer wall, representing as much as 95% of the total heat flux. As the wall resolution is increased, it is expected that the molecular, laminar heat flux will represent the largest fraction of the heat flux.

B. Computational Grid

The computational domain models the full combustion chamber (a cylinder of 286×38.1 mm) and the nozzle (51 mm long with a throat of 8 mm) but a shortened inlet. The very long injector section (152 mm) has been reduced to 50 mm, as can be seen in Fig. 2a, based on independent simulations of the full upstream configuration. The current inlet allows sufficient development of the initial flat profiles with correct bulk flow conditions. The current simulations have been performed on a baseline, multiblock grid. The outer cylindrical block contains $611 \times 87 \times 65$ grid points, while the inner butterfly Cartesian block contains $611 \times 17 \times 17$ grid points (Fig. 2c). Since some of the computational cells in the inlet regions are actually blanked out, the total number of cells is about 3.2 million.

The oxygen post is recessed 0.43 mm from the base of the combustion chamber. At that location, the diameter of the oxygen jet is 5.26 mm. A thin 520 μ sleeve separates it from the annular hydrogen jet near the injection place. The annular gap is 600 μ wide there. The finest resolution is located in the injector posttip region

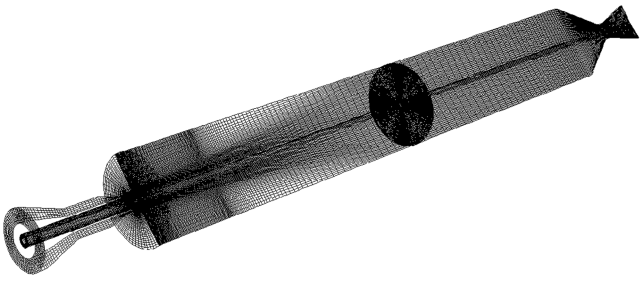

a) Overall view

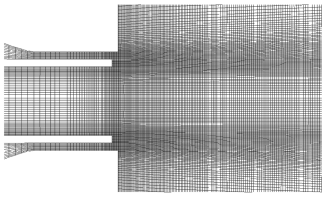

b) Injector near-field

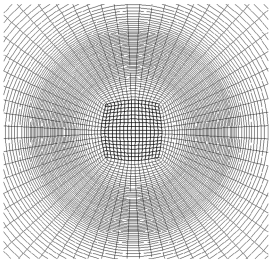

c) Butterfly grid

Fig. 2 Views of the baseline grid for the PSU-RCM1 configuration.

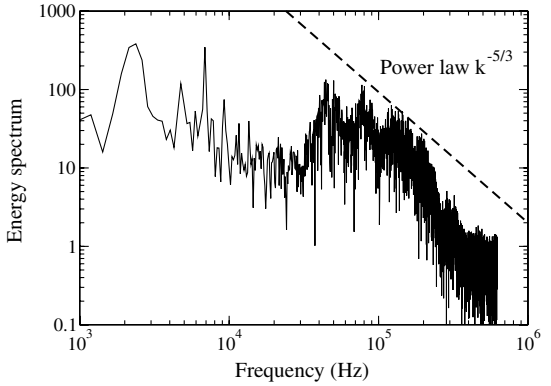

Fig. 3 Resolved kinetic energy spectrum in the injector near field.

($\Delta x_{\text{tip}} = \Delta y_{\text{tip}} = 43$ μ). The resolved kinetic energy spectrum in this region, shown in Fig. 3, demonstrates the recovery of the Kolmogorov $-5/3$ spectrum, indicating sufficient resolution for a proper LES model. While the resolution is coarser in the rest of the combustor, the local Reynolds number is also lower because of the increased viscosity of burned gases. The wall-normal resolution near the outer wall, where the heat flux was measured experimentally, ranges from 0.7 mm in the corner to 0.2 mm further downstream.

To investigate the influence of the grid resolution on the flame structure and on the wall heat flux, a series of axisymmetric simulations was performed since the cost of a full 3-D simulation prohibits such parametric study in three dimensions. Three grids were compared:

1) The first grid is a baseline grid nearly identical to a slice of the 3-D grid, with overall grid dimensions of 610×94.

2) The second grid is a finer grid, where only the resolution near the outer wall was improved ($\Delta y_{\text{wall}} = 100$ μ), with overall grid dimensions of 610×144.

3) The third grid is an even finer grid, where the resolution was improved throughout the combustor, with overall grid dimensions of 916×273 ($\Delta y_{\text{wall}} = 50$ μ and $\Delta x_{\text{tip}} = \Delta x_{\text{tip}} = 20$ μ).

Assuming an azimuthal resolution for these grids in line with the baseline 3-D grid, this would translate into 3-D grids with, respectively, 3.2, 5, and 24 million computational cells. While the 5-million-grid-point simulation could be achieved in a reasonable amount of time on an in-house cluster, the simulation with 24 million points requires a huge increase in computational resources. For comparison, an LES with very high near-wall resolution of the PSU-RCM1 configuration was run as part of the CUIP effort [13] and required more than 2 million CPU hours on 256 million computational cells, with one-third of the cells dedicated to the modeling of the injector upstream from the injection plane.

C. Computational Cost

Very good scaling of the performances have been obtained from 32 processors (the smallest number of processors that can run this case because of memory limitations) to 256 processors, with which most of the simulations have been run. Limited testing shows comparable scaling (above 80% efficiency) for 512 and 1024 processors, but available computational resources did not allow running under such configuration. While the current flow solver has displayed excellent scalability in basic configurations [38], two additional factors help performance in the PSU-RCM1 case: first, the additional processors allow for a more uniform mapping of the computational domain, thus improving the load balancing, and second, the large cost of the chemistry in each cell means the communication between processors represents a small amount of the total computational cost. This simulation has mostly been run on an in-house Intel 3.2 GHz Xeon cluster, but performance on a Cray XT3 is very similar. About 250,000 single-processor hours are required to complete the 20 + ms of simulation used for the statistical analysis reported here.

An issue with the PSU-RCM1 rig is the definition of convergence for the simulations. The volume of the combustor is rather large and

the slow recirculation regions and downstream expansion do not improve the convergence rate of the computations. With the usual definition of flow-through time (FTT: time required for a particle to traverse the domain at a bulk velocity based on the total mass flow and the cross-sectional area), a time of about 8 ms is obtained. The time over which statistics are collected thus corresponds to about 2.5 FTT. However, in the main region of interest (the first third of the combustor), mean velocities are much higher over a smaller length and characteristic times are much smaller. As an estimate, an axial mean velocity of about 200 m/s can be assumed in the first third of the combustor and yields a characteristic time of about $0.125/200 = 0.6$ ms for this region. Consequently, second-order statistics, such as the rms of the velocities, collected over 20 ms are meaningful in the near-field high-speed region but not as much in the recirculation zones or further downstream.

V. Results and Discussion

The same procedure is used to start up the axisymmetric and 3-D simulations. After initializing the combustion chamber with a mixture made of 90% H_2O and 10% OH at 3000 K, reactants are introduced in the domain at their injection temperature and the flame autoignites without any artificial help. Once the flame is anchored in the wake of the injector inner sleeve, 15 ms of physical time are simulated to wash away the influence of the initialization. As mentioned previously, the simulation is then run for at least 20 ms to collect meaningful statistics, especially in the near field. When looking at average quantities for the 3-D simulations, it has to be noted that on top of temporal averaging, spatial averaging over the azimuthal direction has been performed.

A. Steady-State Flowfield

To begin the analysis of the simulations performed in this study, an overview of the PSU-RCM1 flowfield is first presented. The flowfield in the main chamber can be divided into four distinct regions where the dominant physical processes are very different. This is shown in Fig. 4, where zone A corresponds to the very near field of the coaxial injection. It extends downstream up to the end of oxygen core [i.e., around 5 diameters (≈25 mm)] downstream of the injection plane. As will be highlighted later, this zone is dominated by purely diffusive flames. Further downstream, as the oxygen jet breaks down, the flame is no longer simply diffusive as the reactants are being premixed with products. This occurs along the centerline for the oxygen while the hydrogen stream mixes with the products convected by the main recirculation bubble. This bubble, along with the smaller one in the corner of the chamber, defines zone C, which confines the coaxial jet to a narrow tube for the first 10 diameters. In this zone B, the flow first accelerates because of the expansion of the burned gases but then dramatically slows down as the cross-sectional area displaying positive mean axial velocity expands. This flow eventually reattaches to the outer wall and closes the large recirculation bubble. By this time, secondary combustion is almost complete and the mass fraction of intermediate species, such as OH, steadily decreases along the axial direction. The final region D shows very little action up to the convergent–divergent nozzle. From a fluid mechanics point of view, this is a homogeneous lower-Reynolds

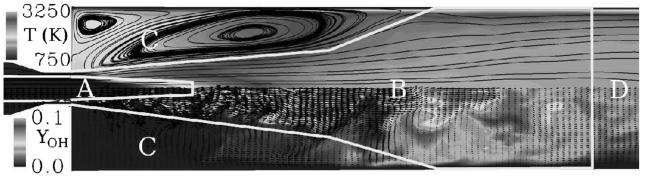

Fig. 4 Division of the flowfield in four main regions, using the underlying time-averaged and instantaneous flowfields as guides. The top half of the figure displays the temporally and spatially averaged streamlines with the temperature, in kelvins, as grayscale contours. The bottom half shows the instantaneous velocity vectors as well as the instantaneous OH mass fraction contours. A detailed description of zones A to D is given in the text.

(Re ≈ 5×10^5) pipe flow, and there is only very limited heat release occurring to perturb this flow. It is expected to display strong axisymmetry both instantaneously and on average.

While the dump combustor configuration has been extensively studied before [39–41], the PSU-RCM1 rig presents a combination of unique features that makes direct comparison with past work difficult: coaxial streams with large velocity ratio, large density difference between the two streams, high levels of heat release. However, it seems likely that the general aspect of the flowfield observed previously would be found again here. Akselvoll and Moin [40] predicted a main recirculation region up to nine step heights after the dump plane, while Afshari et al. [41] observed a shortening of this main recirculation region in reacting flows. In the current case, the reattachment point appears to be around $X = 0.09$ m based on the axial velocity contours, equivalent to about 6.5 step heights. In general, in such a dump combustor configuration, reattachment length is expected to be between 5 and 10 step heights. Akselvoll and Moin [40] also report the secondary vortex in the corner of the chamber. While it is difficult to compare the actual sizes of these recirculation regions with the available literature, the overall flowfield seems in agreement with past experience.

It is interesting to compare the general aspect of the flowfield from the 3-D simulation to the axisymmetric studies mentioned in Sec. IV, where the three grids of increasing resolutions were presented. Figure 5 shows the time-averaged fields of hydrogen mass fractions

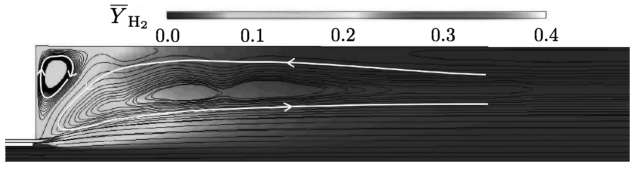

a) Baseline current axi-LES

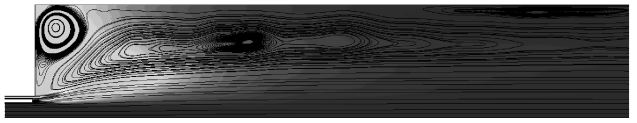

b) Wall-refined current axi-LES

c) Globally refined current axi-LES

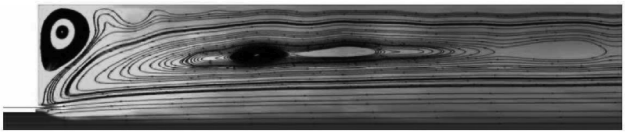

d) Tucker et al. [13] axi-LES

e) Tucker et al. [13] axi-URANS

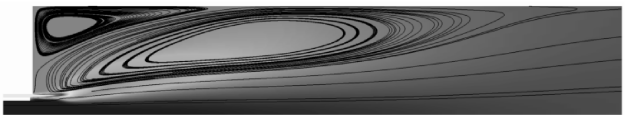

f) Baseline current 3D-LES

Fig. 5 Comparison of the time-averaged (over at least 25 ms for the current simulations) hydrogen mass fraction fields and streamlines for the axisymmetric configuration (first five figures) and the current 3-D configuration.

for these 3 grids, with the flow streamlines overlaid. These streamlines highlight the positive axial flow that only fills about one half of the chamber diameter. This is in stark contrast with the 3-D simulation, where the centerline flow actually reattaches to the outer walls. For the axisymmetric simulations, the outer part of the chamber consists of a large recirculation region that extends from the nozzle to the corner of the chamber. As expected, vortical structures are stronger than in 3-D since there is no third dimension to provide additional dissipation and the oxygen jet core extends much further downstream in axisymmetric flow due to the lack of mixing along the centerline. The same features (longer oxygen core compared with 3-D, recirculation extending over the whole chamber) are also found in other axisymmetric unsteady simulations (LES or unsteady Reynolds-averaged Navier–Stokes) of the PSU-RCM1 configuration [13], as can be seen in Fig. 5.

The grid resolution study indicates that the secondary counter-rotating recirculation bubble in the corner of the chamber gets stronger as the resolution increases, but the overall flow structure remains relatively unchanged. The impact of this recirculation on the wall heat flux is investigated later when the heat flux predictions between 3-D and axisymmetric simulations are compared. Otherwise, the two refined grids show relatively little differences between them, with the wall-refined grid actually displaying slightly higher temperatures (not shown here but it can reach 200 K difference) in the downstream region, along the oxygen jet. The current simulations display a faster consumption of hydrogen than the other unsteady axisymmetric simulations from Tucker et al. [13], and the increased grid resolution also appears to decrease the amount of hydrogen downstream. So, unfortunately, it is impossible to claim that grid independence has been achieved with this axisymmetric study. While the overall flow structure remains the same for all axisymmetric grids, details of mixing and heat transfer have not converged toward a single solution. Moreover, even if grid independence was achieved on axisymmetric studies, the fact that the flow structure differs significantly from the one observed with a comparable 3-D grid prevents an extension of the grid independence to the 3-D case. With current computational resources, a grid convergence study in 3-D is not feasible, however.

B. Influence of the Combustion Closure Model

As mentioned in the formulation section, the current study uses the 21-step 8-species mechanism from Ó Conaire et al. [27]. The numbering of the reaction steps found in Fig. 6 follows the original formulation by Ó Conaire et al. Concerning the numerical integration of the system of differential equations, Fig. 6 shows that for most of the reactions, the characteristic reaction times are below 1 1×10^{-9} s, significantly smaller than the LES time step of about 1×10^{-8} s. As a compromise between the cost and the accuracy of the numerical integration, a simple Euler time integration with 20 subiterations is used instead of solving exactly the system of differential equations.

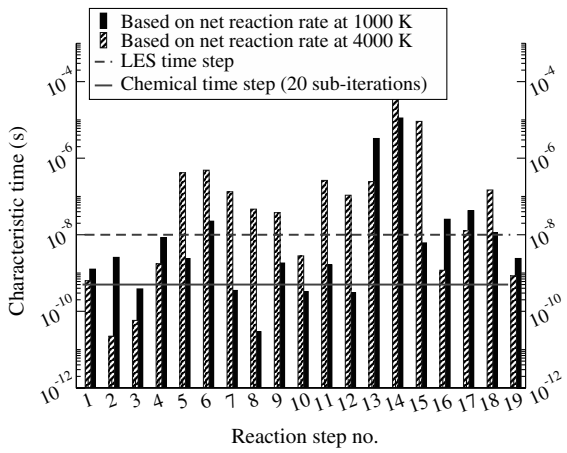

Fig. 6 Comparison of the various chemical characteristic times and the time steps of the flow solver. Longer bars mean larger time scales.

This has the consequence of decoupling different chemical reactions: while the slower reactions are solved exactly, the stiffest reactions are essentially assumed to be in quasi-equilibrium state. This fact is illustrated by Fig. 6, which compares the characteristic chemical times of the various steps in the mechanism at two temperatures: 1000 K (near-field ignition) and 4000 K (upper bound temperature). In the near field, it can be seen that the LES time step is larger than any step except some of the H_2O_2 branching reactions with very large activation energy. However, the simple Euler integration provides a cost-efficient way to capture the majority of the reactions with its time step 20 times smaller than the one for the fluid mechanics. It has to be noted that the times presented here are estimates based on the most likely flow conditions at a given temperature.

Actual characteristic times observed in the flowfield can vary around these values, and very small characteristic times (1×10^{-15} s and smaller) have been observed locally for a short amount of time. This makes the mechanism very difficult to integrate using brute force methods such as solving directly the system of differential equations. A final observation can be made that the hottest regions of the flow present larger characteristic times for the chemistry. These temperatures are reached in a thin layer around the oxygen jet as well as further downstream where the grid resolution is quite coarse. Other solutions, such as the use of artificial neural networks [42], could be investigated in order to find a better compromise between cost and accuracy.

Once the reaction rates, and thus the rates of change of each species, have been evaluated with this laminar closure model, the coupling with the turbulent mixing remains an issue. The configuration of a typical H_2-O_2 coaxial injector is quite unique as it combines relatively high levels of turbulence (at least on the hydrogen side), fast chemistry and small physical dimensions. The resolution of 50 μ found in the shear layer between the two coaxial streams has important consequences on the closure of the combustion process. The smallest resolved eddies approach the thickness of the main reaction region in the near field; thus, the importance of subgrid mixing is diminished. This explains why simple models, such as the eddy breakup model [43], fail to model correctly the combustion in this region. With relatively large mixing times compared with the chemical times, a reaction rate based on the former is unable to sustain the flame under the high strain of the mixing layer. Simulations performed with such a combustion model produce lifted flames because the higher levels of turbulent kinetic energy in the shear layer are not large enough to sustain the near-extinction strain rates (5×10^6 1/s for a hydrogen–oxygen flame extinction strain rate of about 4×10^7 1/s, according to Sohn et al. [44]) observed there.

The level of unresolved kinetic energy, below 10% of the resolved kinetic energy everywhere except in the near-wall region, provides limited amounts of subgrid mixing in the diffusion flame. Moreover, as shown in Fig. 6, the chemistry appears to slow down enough further downstream that the secondary combustion in the slow moving area between zone B and zone D does not require advanced subgrid modeling. It seems that for a configuration such as PSU-RCM1, the small physical dimensions, the high-speed streams, and the fast H_2-O_2 chemistry combine for a situation where turbulent combustion modeling is not as critical to the overall flame dynamics as it is in other engines such as gas turbines. While additional resolution or more advanced modeling is probably required to improve near-wall behavior, the immediate benefits to the capture of the overall flame physics are not clear due to the decoupling of the turbulent and chemical timescales. Another clue to this phenomenon is the qualitative appearance of the flame when the reaction mechanism is solved exactly using direct integration. While that particular simulation was only run for a short amount of time due to its cost, the major species and main radicals (OH, O, and H) fields were mostly identical to the ones obtained with the 20 subiterations scheme. This shows that the chemistry captured at a time step 20 times smaller than the fluid mechanics time step is qualitatively correct and that the implied decoupling, due to the large Damköhler

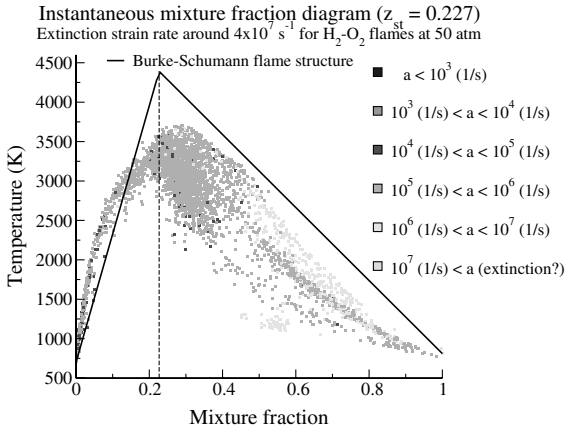

Fig. 7 Scatter plot of the instantaneous diffusion flame structure for temperature versus mixture fraction. The points were extracted from a series of instantaneous snapshots and colored/sized by the local oxidizer strain rate.

number, is justified. Most of the flame is likely under quasi-laminar flamelet regime, which explains why the lack of explicit turbulent combustion closure is not critical in this case.

To further illustrate this point, Fig. 7 displays the diffusion flame structure in the near field of the PSU-RCM1 injector. Using the mixture fraction concept, different instances of the instantaneous flame are compared with a simplified Burke–Schumann flame structure which assumes infinite-rate chemistry (hence the straight lines) and calorically perfect gas (hence the much higher flame temperature predicted). The local strain rate is computed based on oxidizer-side quantities as recommended by Balakrishnan and Williams [45]. It is confirmed that the amount of strain experienced by the flame is large but not close to the theoretical extinction limit. The highest levels of strain are located on the fuel side, which is logical given the low densities on the hydrogen side. As seen earlier, vorticity and strain are limited on the oxidizer-side because of the density gradient and the flame structure on that side is very close to the idealized flame structure. The fuel side of the flame displays much stronger effects from mixing and strain rate, with even some relatively low temperatures associated with mixture fraction not far from the stoichiometric mixture fraction (equal to 0.227 in the PSU-RCM1 case because of the partial premixing of the inlets). These locations are most likely associated with pockets of hydrogen penetrating the oxygen jet, as will be shown later.

C. Heat Flux and Recirculation Zones

The wall heat fluxes predicted by the current simulations given the chosen grids and combustion model are now investigated. The experimental data from Marshall et al. [11] is plotted in Fig. 8 and includes the error bars estimated by the authors. For the 3-D simulation, the heat flux profile has been averaged temporally over 20 ms as well as spatially over the azimuthal direction. The individual fluxes in each azimuthal plane are also plotted in order to represent the scatter of the data.

Far downstream, for $X > 0.1$ m, the decay rate of the heat flux is correctly predicted, even though magnitudes are off by about

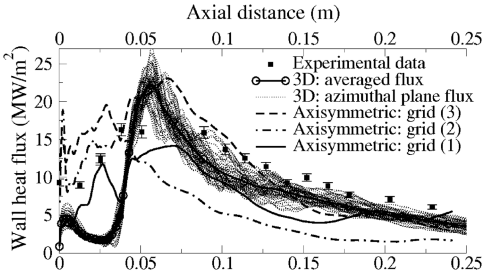

Fig. 8 Comparison of the heat flux predictions for the 3-D and axisymmetric simulations.

20–25%. Upstream, experiments show a plateau of maximum heat flux between $X = 0.04$ m and $X = 0.08$ m, which corresponds to a recirculation flow along the wall in the current simulation. The current LES overpredicts by about 25% the value of that maximum heat flux, even though its location appears to be correctly captured. This might be due to the high levels of subgrid kinetic energy convected from the main shear layer to this wall location. A larger heat flux variability in the azimuthal direction exists around $X = 0.1$ m, as shown by the scatter of the dotted lines on the graph. This is due to the large-scale fluctuations of the reattachment point of the main recirculation bubble. In the corner region, for $X < 0.04$ m, wall heat flux is greatly underpredicted because of a combination of low levels of k^{sgs} and relatively low temperatures. Although some axial heat transfer in the combustor walls cannot be ruled out, it might not be able to explain this discrepancy. Somehow, very little hot products are being convected in this secondary recirculation which remains relatively cold. Analysis of the transient flow evolution in the corner shows that this recirculation is always present but evolves very slowly. Unfortunately, the characteristic time of such recirculation zones is very large and is definitely an issue with respect to the actual convergence of PSU-RCM1 simulations. Also, the shape of the heat flux profile is linked to the k^{sgs} field, as the turbulent heat flux represents a significant portion of the total heat flux with the current grid resolution. The exact near-wall behavior of the subgrid turbulent kinetic energy is difficult to model, especially in the recirculation region where flow reversals and stagnation zones occur.

The heat flux prediction with increasing near-wall resolution in the axisymmetric configuration provides more insight on this behavior. The temporally averaged (over at least 25 ms) heat fluxes for the three axisymmetric grids are also shown ion Fig. 8. With the baseline grid (grid 1) similar to the 3-D grid, a large increase of the heat flux in the corner ($X < 0.05$ m) is observed, so that it almost matches the experimental profile in that region. Downstream, the heat flux is even more underpredicted than with the 3-D grid and overall; since the predicted heat flux is always lower than the experimental one, the global heat load on the chamber walls is significantly underpredicted. However, one could argue that the shape of the heat flux profile is closer to the experimental profile than with the 3-D simulation. But one has to remember that the flow structure obtained with the axisymmetric simulations is very different from the one obtained with the 3-D simulation and that the apparent match obtained here is merely a coincidence. This is proven by the heat flux predictions with the refined grids. As the strength of the recirculation region increases with resolution, the wall heat flux in the corner of the chamber increases and greatly exceeds the experimental values. Further downstream, because of the large recirculation region extending over the whole chamber, the heat flux decays much faster in the axisymmetric configurations than in the 3-D configuration and the experimental profile. Similar trends are observed with the unsteady axisymmetric simulations from Tucker et al. [13], with a reasonable match of the heat flux profile in the near field ($X < 0.05$ m) and a quick decay further downstream. Looking back at Fig. 5, it appears logical that the axisymmetric simulations predict a heat flux maximum closer to the injection plane given the shapes of the recirculation region and the location of the stagnation point between the two recirculation bubbles. That the heat flux predicted in the near field possibly matches the experimental one needs to be carefully evaluated under various grid resolutions. It could be a simple coincidence as it seems to be here with the baseline axisymmetric grid. Only the flow structure of the 3-D simulation predicts correctly the location of the peak heat flux and a moderate improvement of the heat flux magnitude prediction in the near field can be expected from a 3-D simulation using the wall-refined grid. For the current work, as mentioned before, the 3-D simulations will be limited to the baseline grid resolution due to available computational resources, which could explain the underpredicted heat flux in the corner. Tucker et al. [13] also reported on a much-higher-cost 3-D LES simulation for which the flow structure was in reasonable agreement with the current 3-D LES simulation and markedly different from the axisymmetric predictions.

Comparing the averaged flowfield and the instantaneous one at different axial locations yields more insight on these recirculation zones so critical to the heat flux prediction. Figure 9 displays the axisymmetric features of the averaged 3-D flow through the temperature field. The same axisymmetric features are observed through the axial mean velocity field which is not shown here but is accessible elsewhere [46]. On the other hand, Fig. 10 highlights the three-dimensionality of the instantaneous flow. In each figure, the first slice is located in zones A and C, the second slice at the boundary between zone A and zone B, the third and fourth slices in zones B and C, respectively, and the final slice at the beginning of zone D. The central jet and its annular counterpart can clearly be identified in the first slice along with the secondary recirculation in the averaged axial velocity field contours (not shown here for brevity). As the coaxial streams merge and expand, they squeeze both recirculation regions against the walls, resulting in maximum negative velocities near the wall for the main recirculation. At the entrance of zone D, the flow has yet to fully converge toward a perfectly axisymmetric solution. In the first slice of Fig. 9, the hot gases convected by the main recirculation region are clearly visible, forming an annulus of temperature over 2000 K outside of the tight reacting mixing layer. In general, the temperature field appears more homogeneous than the axial velocity field.

The same recirculating hot products can be found in Fig. 10a although they do not form at all a continuous annulus around the main jets. Rather, the secondary recirculation appears connected to the main jets at certain occasions. However, this connection is very limited in space and time and is unable to provide the secondary recirculation zone with significant quantities of fresh hydrogen or hot products from the inner mixing layer. Another difference with the averaged field is that the maximum negative velocities are found in the shear layer between the hydrogen annular jet and the main recirculation region, not near the wall. This is due to the large outer vortices, shown in Fig. 11. The radial extension of the reacting inner mixing layer is also very apparent in Fig. 10, with fingerlike structures reaching far away from the centerline. Temperatures above 3000 K are restricted to this inner mixing layer and its surrounding positive axial flow. They highlight how the oxygen jet breakup is far from being axisymmetric. Unlike a simple jet in dump combustor, the coaxial configuration involves much more fluid transport across the centerline. This makes the use of a fully 3-D formulation even more critical, since an axisymmetric simulation is unable to model a simple confined jet [47].

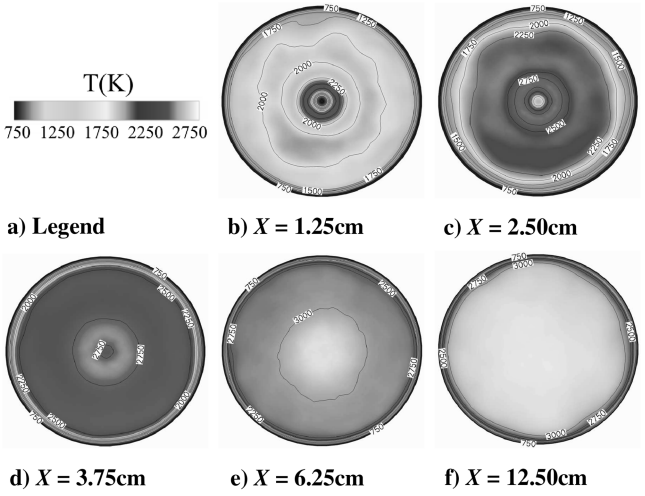

Fig. 9 Averaged temperature field, in kelvins, at various axial locations. The flow is coming toward the reader.

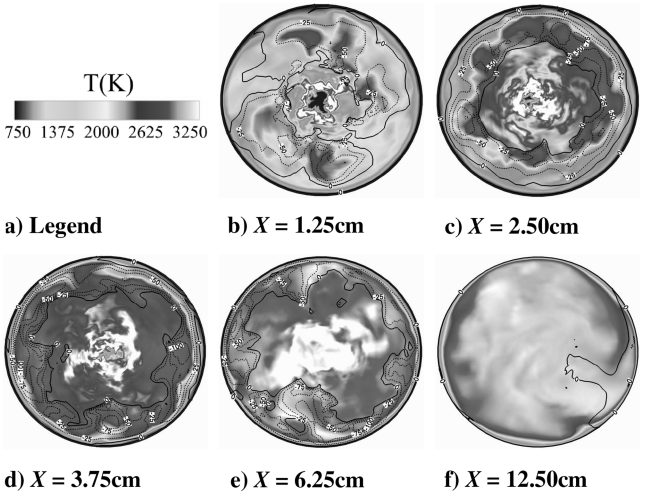

Fig. 10 Instantaneous temperature field, in kelvins, at various axial locations with negative axial velocity contours (dashed lines). Solid black lines delimit recirculation regions. The flow is coming toward the reader.

D. Unsteady Flame Features

Figure 11 focuses on the breakdown of the oxygen jet. From the tip of the oxygen sleeve to about one diameter downstream, a zone without any large coherent vortical structures can be observed. The very high-speed H_2 stream flows straight out of its sleeve while the slow O_2 stream displays only small wrinkles probably caused by the gas expansion near the flame anchor. This anchoring is possible because of a recirculation region right behind the step between the two reactant streams. The recirculation length is two step heights at most. For the remainder of the first diameter, the velocities in this mixing layer remain very low. The flow dynamics then change abruptly when the H_2 annulus starts to get unstable and shed vortices that act as strong perturbation to the oxygen jet. Hydrogen can be seen penetrating the core of the central jet and creating pockets of burned gases further downstream. These pockets appear to be the central mechanism to the oxygen jet break up, more so than pure fluid mechanics shedding. In fact, after three diameters from the injection plane, large-scale vortical structures have either broken down or been significantly damped by gas expansion. The remaining pockets of unburned oxygen are surrounded by mostly diffusive flames that will consume them as they move downstream.

Figure 12 attempts to analyze the flame structure around the oxygen jet through another approach. Following the analysis of Amantini et al. [48], the premixedness index is computed:

$$\alpha = \arccos\left(\frac{\nabla Y_{H_2} \cdot \nabla Y_{O_2}}{\|\nabla Y_{H_2}\| \times \|\nabla Y_{O_2}\|}\right) \tag{9}$$

Expressed in degrees, it can vary between 0 (pure premixed environment) to 180 (pure diffusive environment). This is one of the grayscale contour lines shown in Fig. 12. Since it would be meaningless to plot this quantity everywhere, it is only drawn when the value of the mixing index $\|\nabla Y_{H_2}\| \times \|\nabla Y_{O_2}\|$ is above an arbitrary value. This corresponds to the convoluted area delimited by a thick black line. This effectively highlights where primary combustion between H_2 and O_2 occurs. Indeed, it appears that this primary combustion occurs only at the surface of a tube around the oxygen jet (an open tube, not a closed one as could have been expected, since the overall equivalence ratio is slightly rich). In the case of the PSU-RCM1 injector, the premixedness index lies between 90 and 180, indicating a range from pure diffusion flames (in Fig. 12) to partially premixed flames. It appears that there is a preferred location in the flow where this moderate amount of premixing occurs. As reported previously, the onset of the vortex shedding of the H_2 annulus flow has major repercussions on the injector dynamics. The large-scale structures are able to partially premix the reactants and put the flame under a large strain as seen in next section. But as these vortical structures quickly decay, premixing decreases in the second part of the flame and, once again, the primary combustion between H_2 and O_2 takes place in a purely diffusive fashion.

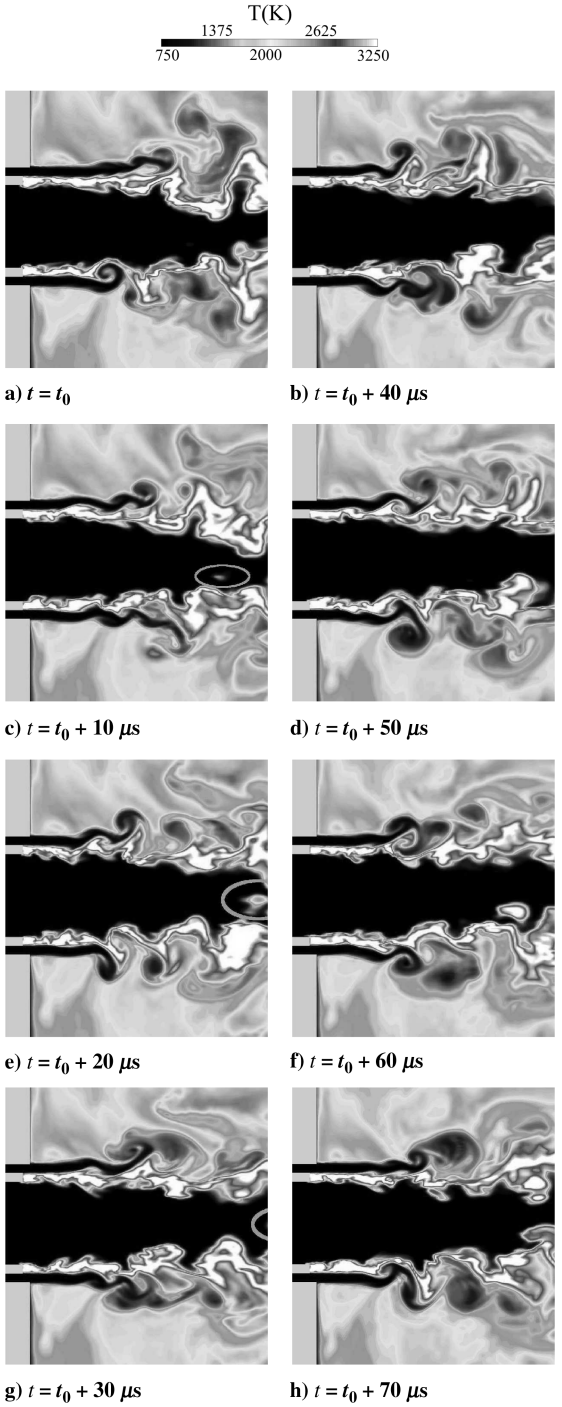

Fig. 11 Successive snapshots of the oxygen jet breakdown process, using grayscale contours of the temperature field. The gray ellipses highlight the penetration of hydrogen into the oxygen jet and the subsequent flame that breaks the tip of the jet.

Figure 12 allows us to identify one more interesting feature for this flame. While the velocity vectors are essentially parallel to the diffusion flame (and thus, the stoichiometric line) over the first couple of diameters, they can become perpendicular to the flame when the jet exhibits large wrinkles further downstream. This can probably be linked to the penetration of H_2 in the oxygen jet reported previously, as the hydrogen gets convected before it even reacts with the oxygen. Finally, as the remaining pockets of oxygen are consumed along the centerline, the process is no longer purely diffusive, since the flame tube remains open over time. On the outside, secondary combustion between the excess hydrogen and the freshly produced OH provides more heat release and explains the peak of temperature observed away from the tip of the oxygen core.

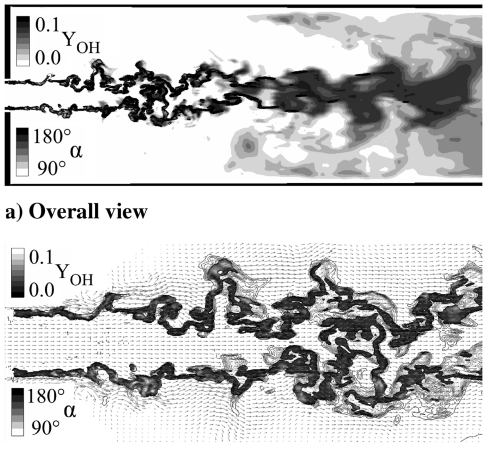

Fig. 12 Visualization of the combustion regime for the diffusion flame around the oxygen jet. In both figures, grayscale contours in the background show OH mass fraction. The grayscale contours inside the convoluted area are delimited by a thick black line to show the premixedness index (angle expressed in degrees) where the mixing index is large enough. Lighter grays indicate partial premixing. The close-up view includes velocity vectors.

E. Other Three-Dimensional and Dynamic Aspects

With Fig. 13, the emphasis is put on the 3-D features of the transient flow while the time-averaged picture remains perfectly axisymmetric. The different slices in Fig. 13a easily relate to the zones previously defined. The first slice, at $X = 0.0125$ m, is in the middle of zone A and displays the large azimuthal variations of the purely diffusive flame. Moving to the second slice at $X = 0.025$ m, the intense and thin diffusion flame has been replaced by the partially premixed flame highlighted previously. Outside the mixing layer, hot burned products alternate with fresh H_2 from the fuel stream, but the further downstream in zone B, the more uniform the outside field becomes. Finally, by $X = 0.125$ m, most of the OH has been consumed (end of the gray isosurface) and the uniform flow enters zone D. The strong azimuthal variations observed in the temperature field have a direct impact on the instantaneous heat flux but over the course of the simulation, these variations rightfully cancel out and the axisymmetric field, shown in Fig. 13b, is obtained. The question is whether or not the full 3-D formulation is then necessary for such a configuration. We believe the oxygen jet breakup requires a centerline free of any velocity constraint. Around the pockets of unburned oxygen, there is significant radial velocity across the centerline, thus a nonaxisymmetric configuration. While the oxygen jet breakup cannot be attributed solely to vortex shedding, fluid mechanics do play an important role in this process. It should be noted that the transient nonaxisymmetric features mentioned previously do not generate any azimuthal, steady instability, such as swirl or tangential acoustic waves. Both recirculation regions remain immobile in the azimuthal direction while pressure traces in four diametrically opposed corners of the chamber show no sign of phase delay. Additional analysis of these pressure signals show a dominant frequency around 2.8 kHz, in the range of frequency for the first longitudinal mode.

Figure 14 highlights the transient nature of the heat transfer to the wall. The simulated heat load (that is, the integral), over the cylindrical part of the chamber, of the wall heat flux displays a 30% peak-to-peak amplitude as it oscillates at a frequency of about 2.4 kHz. This relatively high-frequency oscillation could be of acoustic nature as it seems to match the fundamental longitudinal acoustic mode of the chamber, even though the discrepancy with the pressure spectrum cannot be easily reconciled. It also could be linked to the natural roll-up frequency of the outer shear layer. Cole and Glauser [49] have linked the unsteadiness of the reattachment location to the frequency of the shedding over the dump plane. While it is difficult to choose a reference velocity in the coaxial configuration, an estimate of 200 m/s over a step height of 15 mm

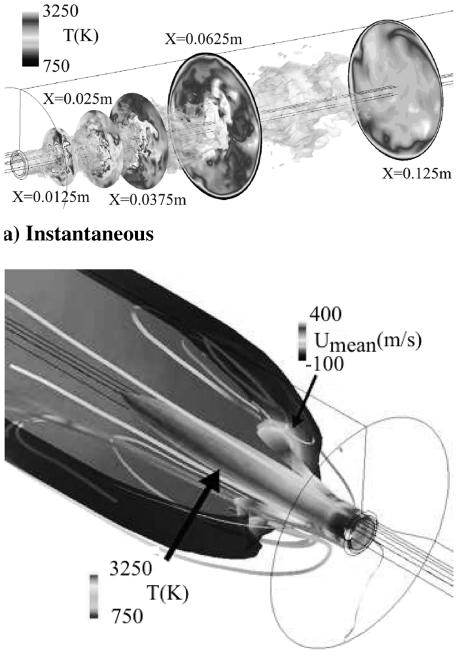

Fig. 13 3-D view of the flowfield. At the top is the instantaneous nonaxisymmetric flow. The gray isosurface is drawn for a mass fraction of OH equal to 0.05. The various slices along the *X* plane show the temperature field with the same scale as in previous figures, from 750 to 3250 K. At the bottom is the time-averaged axisymmetric flowfield. The inner isosurface corresponds to an oxygen mass fraction of 0.25 and is colored by temperature according to the scale shown at the bottom. The outer isosurface corresponds to a temperature of 3000 K and is colored by axial velocity according to the scale shown on the right.

yields a Strouhal number of $(2400 * 0.015)/200 \approx 0.18$, about twice as small as what is reported by Cole and Glauser for a nonreacting axisymmetric jet in a dump combustor. In the end, a combination of these two effects is possible, with the higher frequency acoustic mode interacting with the lower frequency of the roll-up process to produce the intermediate frequency observed in the heat flux signal.

Looking at the transient signal, a low-frequency oscillation, probably below 100 Hz, could also be present. This frequency is probably too low to be explained by a pure acoustic phenomenon inside the main chamber but it also seems unlikely to be related with the chugging of the feed lines, a low-frequency instability observed in full-scale rocket engines as well as in subscale experimental chambers [50]. Such experimental data on the pressure variations at various locations of the combustor should be easier to obtain than a detailed flow visualization and could help obtaining more insight on the physical processes at stake in the chamber. Finally, the difference between the average value of heat load in the experiment and in the current study is slightly less than 20%, which, once again, seems a reasonable result given our assumptions and our near-wall resolution.

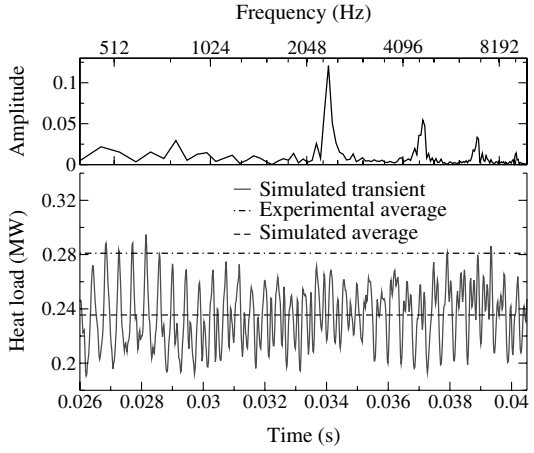

Fig. 14 Analysis of the heat load signal: top chart shows the spectrum of the heat load on the chamber walls, while the bottom graph shows the evolution of the heat load over time and compares the simulated average with the experimental average.

VI. Conclusions

This paper has highlighted the results obtained in the simulation of the PSU-RCM1 rig in the context of the evaluation by NASA of several state-of-the-art CFD techniques. With current available computational resources, the present simulations represent a large effort and the focus is on evaluating the quality of the current approach in capturing realistic flame dynamics and accurate heat flux prediction. The influence of closure models and overall resolution has also been included in this discussion. In general, the current unsteady and 3-D approach appears to successfully produce a physical flowfield, with marked transient and nonaxisymmetric features which eventually produce a truly axisymmetric time-averaged picture. It appears that the PSU-RCM1 configuration considered in this study presents several characteristics that strongly influence the validation effort. On one hand, the size of the combustor and the lack of flow confinement have a negative effect on the convergence time, and thus on the cost of the simulation. On the other hand, it seems that the resolution requirements of the fluid mechanics and the fast chemistry allow for a satisfactory implicit modeling of the turbulent combustion without requiring a more complex and explicit approach.

However, with only the wall heat flux for comparison and validation, it is difficult to draw definite conclusions on the cause of the observed discrepancies. While the current results are encouraging, the fine tuning and definite validation of a given turbulent combustion model for rocket engine flows will require more efforts and more detailed experimental data. Axisymmetric simulations suggest that an improvement in heat flux prediction in the near-field region is possible with a significant refinement of the grid near the outer wall. However, the flow structure predicted by these axisymmetric simulations is markedly different from the one predicted by 3-D simulations and does not seem able to correctly predict the location of the maximum heat flux. Given the current results, future course of action should include more advanced modeling effort as well as additional strategies in order to cut down on the computational cost. On the modeling front, given the specifics of the PSU-RCM1 configuration, the LEM closure could provide a better simulation of the complex flame structure detailed in this paper. However, given the overall cost, the LES–LEM formulation could be first applied to simpler cases such as the very near field of a coaxial injector, without any constraints based on the size of the domain or the near-wall resolution. It would either confirm or infirm the assumptions made in the current study about the decoupling between the turbulence and the chemistry. Such a study, comparing different methods to compute the filtered reaction rate under realistic rocket conditions is planned in the future. It would include different techniques to solve the reaction mechanism (direct integration, Euler integration, and neural networks) and evaluate closure models such as the one used in the current work or one based on a turbulent neural network [42]. Similarly, the inclusion of a dynamic closure for the turbulent kinetic energy as well as better wall modeling could improve the prediction of the wall heat flux, mostly controlled by the unresolved kinetic energy with the current grid resolution. The added cost could be countered by grid coarsening methods and the aforementioned use of neural networks.

Nonetheless, the current 3-D LES formulation, with its hybrid solver, appears capable of predicting the overall physics of the flow and represents a powerful analysis tool that can be extended to other configurations related to rocket engines, especially under conditions where real gas effects could be dominant.

Acknowledgments

This work was sponsored by the NASA Constellation University Institutes Project under grant NCC3-989, with Claudia Meyer as the project manager. The authors would also like to thank Kevin Tucker for his support. Simulations were conducted on the Computational Combustion Laboratory's Linux clusters.

References

[1] Tucker, P. K., Klem, M. D., Smith, T. D., Farhangi, S., Fisher, S. C., and Santoro, R. J., "Design of Efficient GO_2/GH_2 Injectors: A NASA, Industry and University Cooperative Effort," 33rd AIAA/ASME/SAE/ASEE Joint Propulsion Conference, AIAA Paper 1997-3350, July 1997.

[2] Habiballah, M., Orain, M., Grisch, F., Vingert, L., and Gicquel, P., "Experimental Studies of High-Pressure Cryogenic Flames on the Mascotte Facility," *Combustion Science and Technology*, Vol. 178, No. 1-3, 2006, pp. 101–128. doi:10.1080/00102200500294486

[3] Cheng, G. C., and Farmer, R., "Real Fluid Modeling of Multiphase Flows in Liquid Rocket Engine Combustors," *Journal of Propulsion and Power*, Vol. 22, No. 6, Nov.–Dec. 2006, pp. 1373–1381. doi:10.2514/1.17272

[4] Smith, J. J., Schneider, G., Suslov, D., Oschwald, M., and Haidn, O., "Steady-State High Pressure LO_x/H_2 Rocket Engine Combustion," *Aerospace Science and Technology*, Vol. 11, No. 1, 2007, pp. 39–47. doi:10.1016/j.ast.2006.08.007

[5] Mayer, W. O. H., Ivancic, B., Schik, A., and Hornung, U., "Propellant Atomization and Ignition Phenomena in Liquid Oxygen/Gaseous Hydrogen Rocket Combustors," *Journal of Propulsion and Power*, Vol. 17, No. 4, 2001, pp. 794–799. doi:10.2514/2.5835

[6] Matsuyama, S., Shinjo, J., Mizobuchi, Y., and Ogawa, S., "A Numerical Investigation on Shear Coaxial LOX/GH_2 Jet Flame at Supercritical Pressure," 44th Aerospace Sciences Meeting and Exhibit, AIAA Paper 2006-761, Jan. 2006.

[7] Knab, O., and Preclik, D., "Test Case RCM-3: EADS-ST Subscale Chamber," *3rd International Workshop Rocket Combustion Modeling*, Vernon, France, SNECMA, Villaroche, France, March 2006, pp. 20–26.

[8] Masquelet, M., Menon, S., Jin, Y., and Friedrich, R., "Simulation of Unsteady Combustion in a LOX-GH_2 Fueled Rocket Engine," *Aerospace Science and Technology*, Vol. 13, No. 8, Dec. 2009, pp. 466–474. doi:10.1016/j.ast.2009.07.005

[9] Lin, J., West, J. S., Williams, R. W., Tucker, P. K., and Chenoweth, J. D., "CFD Code Validation of Wall Heat Fluxes for a GO_2/GH_2 Single Element Combustor," 41st AIAA/ASME/SAE/ASEE Joint Propulsion Conference and Exhibit, AIAA Paper 2005-4524, July 2005.

[10] Duwig, C., and Fuchs, L., "Large Eddy Simulation of a H_2/N_2 Lifted Flame in a Vitiated Co-Flow," *Combustion Science and Technology*, Vol. 180, No. 3, 2008, pp. 453–480. doi:10.1080/00102200701741327

[11] Marshall, W. M., Pal, S., Woodward, R. D., and Santoro, R. J., "Benchmark Wall Heat Flux Data for a GO_2/GH_2 Single Element Combustor," 41st AIAA/ASME/SAE/ASEE Joint Propulsion Conference and Exhibit, AIAA Paper 2005-3572, July 2005.

[12] Conley, A., Vaidyanathan, A., and Segal, C., "Heat Flux Measurements for a GO_2/GH_2 Single- Element, Shear Injector," *Journal of Spacecraft and Rockets*, Vol. 44, No. 3, 2007, pp. 633–639. doi:10.2514/1.26678

[13] Tucker, P. K., Menon, S., Merkle, C. L., Oefelein, J. C., and Yang, V., "Validation of High-Fidelity CFD Simulations for Rocket Injector Design," 44th AIAA/ASME/SAE/ASEE Joint Propulsion Conference and Exhibit, AIAA Paper 2008-5226, July 2008.

[14] Erlebacher, G., Hussaini, M. Y., Speziale, C. G., and Zang, T. A., "Toward the Large-Eddy Simulation of Compressible Turbulent Flows," *Journal of Fluid Mechanics*, Vol. 238, No. 1, 1992, pp. 155–185. doi:10.1017/S0022112092001678

[15] Palle, S., Nolan, C., and Miller, R. S., "On Molecular Transport Effects in Real Gas Laminar Diffusion Flames at Large Pressure," *Physics of Fluids*, Vol. 17, No. 10, Oct. 2005, Paper 103601.doi:10.1063/1.1990198

[16] Mahle, I., Sesterhenn, J., and Friedrich, R., "Turbulent Mixing in Temporal Compressible Shear Layers Involving Detailed Diffusion Processes," *Journal of Turbulence*, Vol. 8, No. 1, 2007, pp. 1–21. doi:10.1080/14685240600806256

[17] Fureby, C., *On Modeling of Unsteady Combustion Utilizing Continuum Mechanical mixture Theories and Large Eddy Simulations*, Ph.D. Thesis, Lund Inst. of Technology, Lund, Sweden, 1995.

[18] Veynante, D., and Poinsot, T., "Reynolds Averaged and Large Eddy Simulation Modeling for Turbulent Combustion," *New Tools in Turbulence Modeling*, edited by O. Metais, and J. Ferziger, Les Editions De Physique, Springer, Berlin, 1996.

[19] Menon, S., and Patel, N., "Subgrid Modeling for Simulation of Spray Combustion in Large-Scale Combustors," *AIAA Journal*, Vol. 44, No. 4, April 2006, pp. 709–723. doi:10.2514/1.14875

[20] Menon, S., and Kim, W.-W., "High Reynolds Number Flow Simulations Using the Localized Dynamic Subgrid-Scale Model," AIAA Paper 1996-0425, 1996.

[21] Kim, W.-W., Menon, S., and Mongia, H. C., "Large Eddy Simulations of a Gas Turbine Combustor Flow," *Combustion Science and Technology*, Vol. 143, No. 1, 1999, pp. 25–62. doi:10.1080/00102209908924192

[22] Chakravarthy, V. K., and Menon, S., "Subgrid Modeling of Premixed Flames in the Flamelet Regime," *Flow, Turbulence and Combustion*, Vol. 65, No. 2, 2001, pp. 133–161. doi:10.1023/A:1011456218761

[23] Aouissi, M., Bounif, A., and Bensayah, K., "Scalar Turbulence Model Investigation with Variable Turbulent Prandtl Number in Heated Jets and Diffusion Flames," *International Journal of Heat and Mass Transfer*, Vol. 44, No. 9, 2008, pp. 1065–1077. doi:10.1007/s00231-007-0350-8

[24] Volkov, K. N., "Large Eddy Simulation of a Nonisothermal Turbulent Jet Flowing out into Submerged Space," *High Temperature*, Vol. 46, No. 5, 2008, pp. 630–638. doi:10.1134/S0018151X08050076

[25] Gordon, S., and McBride, B. J., "Computer Program for Calculation of Complex Chemical Equilibrium Compositions and Applications," NASA, Reference Publ. 1311, 1994.

[26] Wilke, C. R., "Diffusional Properties of Multicomponent Gases," *Chemical Engineering Progress*, Vol. 46, No. 2, 1950, pp. 95–104.

[27] Ó Conaire, M., Curran, H. J., Simmie, J. M., Pitz, W. J., and Westbrook, C. K., "A Comprehensive Modeling Study of Hydrogen Oxidation," *International Journal of Chemical Kinetics*, Vol. 36, No. 11, 2004, pp. 603–622. doi:10.1002/kin.20036

[28] Tramecourt, N., Masquelet, M., and Menon, S., "Large-Eddy Simulation of Unsteady Wall Heat Transfer in a High Pressure Combustion Chamber," 41st AIAA/ASME/SAE/ASEE Joint Propulsion Conference and Exhibit, AIAA Paper 2005-4124, 2005.

[29] Masquelet, M., "Simulations of a Sub-Scale Liquid Rocket Engine: Transient Heat Transfer in a Real Gas Environment," M.S. Thesis, Georgia Inst. of Technology, Atlanta, Dec. 2006.

[30] Tucker, P. K., Rybak, J. A., Hulka, J., Jones, G. W., Nesman, T., and West, J. S., "The NASA Constellation University Institutes Project: Thrust Chamber Assembly Virtual Institute," 42nd AIAA/ASME/SAE/ASEE Joint Propulsion Conference and Exhibit, AIAA Paper 2006-4524, 2006.

[31] Tucker, P. K., Menon, S., Merkle, C. L., Oefelein, J. C., and Yang, V., "An Approach to Improved Credibility of CFD Simulations for Rocket Injector Design," 43rd AIAA/ASME/SAE/ASEE Joint Propulsion Conference and Exhibit, AIAA Paper 2007-5572, July 2007.

[32] Santoro, R. J., and Pal, S., "Test Case RCM-1: Penn State Preburner Combustor," *3rd International Workshop Rocket Combustion Modeling*, Vernon, France, SNECMA, Villaroche, France, March 2006, pp. 1–9.

[33] Preclik, D., Knab, O., Görgen, J., and Hagemann, G., "Simulation and Analysis of Thrust Chamber Flowfields: Cryogenic Propellant Rockets," *Liquid Rocket Thrust Chambers: Aspects of Modeling, Analysis, and Design*, Vol. 200, Progress in Astronautics and Aeronautics, AIAA, Reston, VA, 2004, pp. 527–551, Chap. 15.

[34] Genin, F., Fryxell, B., and Menon, S., "Hybrid Large-Eddy Simulation of Detonation in Reactive Mixtures," *Proceedings of the 20th International Conference on Detonations, Explosions and Shock Waves*, Montreal, Canada, Aug. 2005.

[35] Génin, F., and Menon, S., "Studies of Shock/Turbulent Shear Layer Interaction Using Large-Eddy Simulation," *Computers and Fluids*, Vol. 39, No. 5, May 2010, pp. 800–919. doi:10.1016/j.compfluid.2009.12.008

[36] Toro, E. F., Spruce, M., and Speares, W., "Restoration of the Contact Surface in the HLL Riemann Solver," *Shock Waves*, Vol. 4, No. 1, 1994, pp. 25–34. doi:10.1007/BF01414629

[37] Tannehill, J. C., Anderson, D. A., and Pletcher, R. H., *Computational Fluid Mechanics and Heat Transfer*, 2nd ed., Taylor and Francis, Washington, D.C., 1997.

[38] Masquelet, M., Génin, F., and Menon, S., "Update to the 107.leslie3-D code for the SPEC MPI2007 Benchmark," Georgia Inst. of Technology, Computational Combustion Lab., TR 2008-004-1, Atlanta, GA, 2008.

[39] Morrison, G. L., Tatterson, G. B., and Long, M. W., "Three-Dimensional Laser Velocimeter Investigation of Turbulent, Incompressible Flow in an Axisymmetric Sudden Expansion," *Journal of Propulsion and Power*, Vol. 4, No. 6, Nov.–Dec. 1988, pp. 533–540. doi:10.2514/3.23097

[40] Akselvoll, K., and Moin, P., "Large-Eddy Simulation of Turbulent Confined Coannular Jets," *Journal of Fluid Mechanics*, Vol. 315, No. 1, 1996, pp. 387–411. doi:10.1017/S0022112096002479

[41] Afshari, A., Jaberi, F. A., and Shih, T., "Large-Eddy Simulations of Turbulent Flows in an Axisymmetric Dump Combustor," *AIAA Journal*, Vol. 46, No. 7, July 2008, pp. 1576–1592. doi:10.2514/1.25467

[42] Sen, B. A., Hawkes, E. R., and Menon, S., "Large Eddy Simulation of Extinction and Reignition with Artificial Neural Networks Based Chemical Kinetics," *Combustion and Flame*, Vol. 157, No. 3, 2010, pp. 566–578. doi:10.1016/j.combustflame.2009.11.006

[43] Brink, A., Mueller, C., Kilpinen, P., and Hupa, M., "Possibilities and Limitations of the Eddy Break- Up Model," *Combustion and Flame*, Vol. 123, Nos. 1–2, 2000, pp. 275–279. doi:10.1016/S0010-2180(00)00146-2

[44] Sohn, C. H., Chung, S. H., Lee, S. R., and Kim, J. S., "Structure and Acoustic-Pressure Response of Hydrogen–Oxygen Diffusion Flames at High Pressure," *Combustion and Flame*, Vol. 115, No. 3, 1998, pp. 299–312. doi:10.1016/S0010-2180(98)00007-8

[45] Balakrishnan, G., and Williams, F. A., "Turbulent Combustion Regimes for Hypersonic Propulsion Employing Hydrogen-Air Diffusion Flames," *Journal of Propulsion and Power*, Vol. 10, No. 3, 1994, pp. 434–437. doi:10.2514/3.23754

[46] Masquelet, M., and Menon, S., "Large Eddy Simulation of Flame-Turbulence Interactions in a GH_2-GO_2 Shear Coaxial Injector," 44th AIAA/ASME/SAE/ASEE Joint Propulsion Conference and Exhibit, AIAA Paper 2008-5030, 2008.

[47] Schlüter, J. U., "Influence of Axisymmetric Assumptions on Large Eddy Simulations of a Confined Jet and a Swirl Flow," *International Journal of Computational Fluid Dynamics*, Vol. 18, No. 3, April 2004, pp. 235–246. doi:10.1080/10618560310001624484

[48] Amantini, G., Frank, J. H., Bennett, B. A. V., Smooke, M. D., and Gomez, A., "Comprehensive Study of the Evolution of an Annular Edge Flame During Extinction and Reignition of a Counterflow Diffusion Flame Perturbed by Vortices," *Combustion and Flame*, Vol. 150, No. 4, 2007, pp. 292–319. doi:10.1016/j.combustflame.2007.04.010

[49] Cole, D., and Glauser, M., "Applications of Stochastic Estimation in the Axisymmetric Sudden Expansion," *Physics of Fluids*, Vol. 10, No. 11, Nov. 1998, pp. 2941–2949. doi:10.1063/1.869814

[50] Tamura, H., Sakamoto, H., Takahashi, M., Sasaki, M., Onodera, T., Tomita, T., and Mayer, W. O. H., "Observation of LOX/Hydrogen Combustion Flame in a Rocket Chamber During Chugging Instability," 39th AIAA/ASME/SAE/ASEE Joint Propulsion Conference and Exhibit, AIAA Paper 2003-4756, July 2003.

J. Oefelein
Associate Editor